Polarimetric measurements of single-photon geometric phases

O. Ortíz[1], Y. Yugra[1], A. Rosario[1], J. C. Sihuincha[1], J. C. Loredo[2], M. V. Andrés[3] and F. De Zela[1]
[1] *Departamento de Ciencias, Sección Física, Pontificia Universidad Católica del Perú, Apartado 1761, Lima, Peru.*
[2] *Centre for Engineered Quantum Systems, Centre for Quantum Computer and Communication Technology, and School of Mathematics and Physics, University of Queensland, 4072 Brisbane, QLD, Australia*
[3] *Departamento de Física Aplicada y Electromagnetismo, Universidad de Valencia, c/Dr. Moliner 50, Burjassot, Valencia, Spain*

We report polarimetric measurements of geometric phases that are generated by evolving polarized photons along non-geodesic trajectories on the Poincaré sphere. The core of our polarimetric array consists of seven wave plates that are traversed by a single photon beam. With this array any $SU(2)$ transformation can be realized. By exploiting the gauge invariance of geometric phases under $U(1)$ local transformations, we nullify the dynamical contribution to the total phase, thereby making the latter coincide with the geometric phase. We demonstrate our arrangement to be insensitive to various sources of noise entering it. This makes the single-beam, polarimetric array a promising, versatile tool for testing robustness of geometric phases against noise.

PACS numbers: 03.65.Vf, 03.67.Lx, 42.65.Lm

arXiv:1510.03802v1 [quant-ph] 13 Oct 2015

I. INTRODUCTION

Even though experiments testing different properties of geometric phases are continuously reported, theoretical developments can expand at such a spanking pace that experimental testing can be left behind for a while. This seems to be the case with the subject of geometric phases. Since Berry's seminal work [1], which brought to light the appearance of geometric phases in adiabatically evolving, cyclic quantum processes, there have been considerable generalizations of the subject. From Hannay angles in the classical domain [2] to geometric phases in mixed quantum states subjected to non-unitary and non-cyclic evolutions [3–7], the original concept of geometric phases has been widely expanded. Experimental testing is required not only because of fundamental reasons lying at the basis of all empirical sciences, but because experimental input can help us in finding the answer to open questions. Notably, the question about a proper, self-consistent definition of a geometric phase for non-unitary evolutions still remains open [8–13]. Similarly, the kind of robustness that geometric phases might have against decohering mechanisms is also an open question of utmost importance, particularly in the realm of quantum computation [14]. It is thus useful to explore as much experimental techniques as possible. One should not refrain from mirroring experiments already performed with one technique and conduct similar experiments based on another independent technique. This can provide not only new insights, but an enlarged versatility as well. Geometric phases are particularly well suited for such an approach, as they notoriously appear in the evolution of two-level systems. Such systems can be realized under manifold situations, quantal and classical ones. The drawbacks of one technique could then be replaced by some advantages of the other. For example, the physical realization of the qubit as a spin one-half particle, e.g. a neutron, has its counterpart in the realization of the qubit as a polarized photon. While as a source of the former one needs a nuclear reactor, as a source of the latter it suffices a diode-laser. On the other hand, the versatility reached in experiments with neutrons can outperform the one reached with their optical counterparts. A challenge is thereby put on the latter, as to how to improve their versatility. We have addressed such a challenge in the present work. We report on experiments performed with single photons, which to some extent mirror previous experiments that were conducted with neutrons [15–18]. Our experiments put under test theoretical predictions about $SU(2)$ evolutions along non-geodesic paths. Using neutrons, experiments along these lines have been conducted by exploiting the advantages offered by polarimetric techniques. In contrast to interferometric techniques [19], polarimetric ones have an intrinsic robustness, because they require a single beam [20]. The challenge posed here, however, is how to manipulate two coherently superposed states that are not spatially separated. In interferometry, the (binary) path degree of freedom can be used together with an "internal" degree of freedom, e.g. the spin, that is carried along by the particle. In polarimetry instead, there is only one path. One must then figure out how to deal with this restriction and nevertheless reach a versatility that is comparable to that of interferometry. The latter offers, for example, the possibility of spin-path entanglement. In neutron polarimetry, energy-polarization and even a tripartite energy-polarization-momentum entanglement have been achieved [21]. Although an all-optical version of the latter seems difficult to implement, there are other features that can be exploited with advantage in optical polarimetry. We show here how to exploit the invariance of geometric phases under local gauge transformations [22], in order to nullify the dynamical part of the total (Pancharatnam) phase [23], thereby making this phase coincide with the geometric phase. What is meant by gauge invariance is the invariance under the change $|\psi(s)\rangle \to |\psi'(s)\rangle = \exp\left(i\alpha(s)\right)|\psi(s)\rangle$ of

an unitarily evolving state $|\psi(s)\rangle$. By exploiting this invariance, one can nullify the dynamical contribution to the total phase $\Phi_P = \arg\langle\psi(s_1)|\psi(s_2)\rangle$ between an initial and a final state, $|\psi(s_1)\rangle$ and $|\psi(s_2)\rangle$, respectively. What remains after elimination of the dynamical part is the purely geometric contribution Φ_g to the total phase $\Phi_P = \Phi_g + \Phi_{dyn}$. The $SU(2)$ evolutions we have addressed are those of the type given by $U_n(\theta,\varphi,s) = \exp\left[-is\mathbf{n}(\theta,\varphi)\cdot\boldsymbol{\sigma}/2\right]$. Here, $\mathbf{n}$ is a unit vector, $\boldsymbol{\sigma}$ is the triple of Pauli matrices and s is the rotation angle (on the Bloch or Poincaré sphere). We could generalize our approach so as to deal with unit vectors that depend on s, but we have focused on cases with a fixed $\mathbf{n}$. We also restricted ourselves to deal with pure single-photon states. These restrictions are justified in view of the extension already achieved by considering the production of geometric phases in systems subjected to transformations $U_n(\theta,\varphi,s)$ of the above type. Previous experimental tests were restricted to particular trajectories that a system follows when subjected to some special transformations [15, 17, 18]. The cases we address here let us study what happens when we lift these restrictions. In such a case, a series of features shows up that is worthwhile to analyze before undertaking a systematic investigation of, say, the sensitivity of geometric phases to environmental influences. A main motivation of the present work was to analyze and to explain the appearance of the aforementioned features. This opens the way for using this array as a basic component for testing the impact of decohering mechanisms.

II. POLARIMETRY

The standard procedure to exhibit the relative phase between two states is to make them interfere and then record the intensity of the interfering pattern by varying the relative phase. An archetypical setup for doing this is a Mach-Zehnder interferometer. Expressed in the language of quantum gates [24], such a device consists of two Hadamard gates – i.e., two beam splitters – and a phase-shifter. A Hadamard gate can be represented in terms of Pauli matrices as $U_H = (\sigma_x + \sigma_z)/\sqrt{2}$, while the phase-shifter can be represented as $U_\phi = \exp(-i\phi\sigma_z/2)$. Hereby, we establish a one-to-one correspondence between the eigenvectors $|\pm\rangle$ of σ_z and the two paths of the interferometer. The action of the interferometer on an input state $|+\rangle$ is thus given by $|+\rangle \to U_H U_\phi U_H |+\rangle$. The output intensity that is recorded at, say, a $|+\rangle$-detector, reads $I = |\langle+| U_H U_\phi U_H |+\rangle|^2 = (1+\cos\phi)/2$. Now, instead of assigning the states $|\pm\rangle$ to the two possible paths of the interferometer, we can make them correspond to the horizontal and vertical polarization states of a single light-beam. We thereby change from interferometry to polarimetry. In the latter, the action of U_ϕ and U_H can be realized with the help of quarter-wave (Q) and half-wave (H) plates. Indeed, we have that $U_\phi = Q(\pi/4)H((\phi-\pi)/4)Q(\pi/4)$ and $U_H = -iH(\pi/8)$. The arguments in H and Q refer to the angles made by the plate's major axis and the vertical direction. Up to a global phase, the action of the Mach-Zehnder interferometer can then be mirrored in polarization space by letting a polarized light-beam traverse a gadget that consists of a couple of aligned retarders. In the present case, such an array is given by $Q(\pi/2)H((2\pi-\phi)/4)Q(\pi/2)$. This last expression is obtained by using $Q(\alpha)H(\beta) = H(\beta)Q(2\beta-\alpha)$ and $Q(\alpha)H(\beta)H(\gamma) = Q(\alpha+\pi/2)H(\alpha-\beta+\gamma-\pi/2)$. Hence, by setting a horizontal polarizer before a detector and recording the intensity as a function of ϕ, we get a pattern that looks the same as the interferogram produced with the Mach-Zehnder device. Polarimetry has the great advantage of being largely insensitive to those perturbations that in the case of interferometry lead to random phase shifts. On the other hand, the states $|\pm\rangle$ cannot be individually addressed, as they are no longer spatially separated from one another, as it occurs in interferometry. We must then find a way to extract the desired information by adequately projecting the manipulated states before detection. In the case of geometric phases this is indeed possible, as we show next.

Following a similar procedure as the one introduced by Wagh and Rakhecha [20] – thereby extending to single photons some techniques already employed with classical light [25–27] – we consider an initial, horizontally polarized state $|h\rangle$ and submit it to a $\pi/2$-rotation around the x-axis. This produces a circularly polarized state $\left(|h\rangle - i\,|v\rangle\right)/\sqrt{2}$. By submitting this state to the transformation $\exp\left(-i\phi\sigma_z/2\right)$ we get $V|h\rangle \equiv \exp\left(-i\phi\sigma_z/2\right)\exp\left(-i\pi\sigma_x/4\right)|h\rangle$, which is the state $\left(|h\rangle - ie^{i\phi}\,|v\rangle\right)/\sqrt{2}$, up to a global phase. Hence, we have generated a relative phase-shift $\phi-\pi/2$ between $|h\rangle$ and $|v\rangle$. If we now apply $U \in SU(2)$, then we obtain $UV|h\rangle = \left(e^{-i\phi/2}U|h\rangle - ie^{i\phi/2}U|v\rangle\right)/\sqrt{2}$. We are interested in $U_n(\theta,\varphi,s) = \exp\left[-is\mathbf{n}(\theta,\varphi)\cdot\boldsymbol{\sigma}/2\right]$ and the geometric phase that this transformation generates. We recall that the geometric phase is given by [22]

$$\Phi_g(\mathcal{C}) = \arg\langle\psi(0)|\psi(s)\rangle - \Im\int_0^s \langle\psi(s')|\dot{\psi}(s')\rangle ds', \tag{1}$$

for a path $\mathcal{C}$ joining the initial state $|\psi(0)\rangle$ with the final state $|\psi(s)\rangle$. As already said, Φ_g is invariant under local gauge transformations. We exploit this property in order to nullify the dynamical contribution to Φ_g. That is, we choose a gauge transformation $|\psi(s)\rangle \to |\psi'(s)\rangle = \exp\left(i\alpha(s)\right)|\psi(s)\rangle$ so that $\langle\psi'(s)|\dot{\psi}'(s)\rangle = 0$. In other words, instead of applying $U_n(\theta,\varphi,s)$ we apply $\exp\left[i\alpha(s)\right]U_n(\theta,\varphi,s)$ and measure the total phase $\arg\langle\psi(0)|\psi(s)\rangle$. In the present case, this can be achieved by setting $\alpha(s) = s\,\langle+|\,\mathbf{n}\cdot\boldsymbol{\sigma}\,|+\rangle/2$. That is, we seek to implement the transformation

$|h\rangle \to U_n V |h\rangle = \left(e^{-i\gamma/2} U_n |h\rangle - i e^{i\gamma/2} U_n |v\rangle\right)/\sqrt{2}$, where $\gamma(s) = \phi - \alpha(s)$. We can realize this with the help of wave plates. To begin with, U_n can be implemented with a gadget proposed by Simon and Mukunda [28], which is given by

$$U_n(\theta, \varphi, s) = Q\left(\frac{\pi+\varphi}{2}\right) Q\left(\frac{\theta+\varphi}{2}\right) H\left(\frac{-\pi+\theta+\varphi}{2} + \frac{s}{4}\right) Q\left(\frac{\theta+\varphi}{2}\right) Q\left(\frac{\varphi}{2}\right). \tag{2}$$

The rotation axis is here given by $\mathbf{n} = (\sin\theta\cos\varphi, \sin\theta\sin\varphi, \cos\theta)$ and the Pauli matrices are defined according to the convention that is commonly employed in optics. That is, the diagonal matrix in the basis $\{|h\rangle, |v\rangle\}$ of horizontally and vertically polarized states, is σ_x. The other two Pauli matrices follow from cyclically completing the change $\sigma_z \to \sigma_x$. With this choice, our gauge is given by

$$\alpha(s) = \frac{s}{2}\sin\theta\cos\varphi. \tag{3}$$

On the other hand, $V(\gamma) = e^{-i\gamma\sigma_z/2} e^{-i\pi\sigma_x/4}$ can be implemented as $V(\gamma) = Q(\pi/4) H\left((\gamma-\pi)/4\right) H(\pi/4)$. The total transformation is thus

$$U_{tot} \equiv V^\dagger U_n V = H\left(-\frac{\pi}{4}\right) H\left(\frac{\gamma+\pi}{4}\right) Q\left(-\frac{\pi}{4}\right) U_n(\theta, \varphi, s) Q\left(\frac{\pi}{4}\right) H\left(\frac{\gamma-\pi}{4}\right) H\left(\frac{\pi}{4}\right). \tag{4}$$

Applying as before relations like $Q(\alpha)H(\beta) = H(\beta)Q(2\beta-\alpha)$, $Q(\alpha)H(\beta)H(\gamma) = Q(\alpha+\pi/2)H(\alpha-\beta+\gamma-\pi/2)$, etc., we reduce the above array to one that consists of seven plates:

$$\begin{aligned} U_{tot}(\theta, \varphi, \phi, s) \;=\; & Q\left(\frac{\pi}{4} - \frac{\gamma_\phi(s)}{2}\right) Q\left(-\pi - \frac{\varphi}{2} - \frac{\gamma_\phi(s)}{2}\right) Q\left(\frac{\pi-\theta-\varphi}{2} - \frac{\gamma_\phi(s)}{2}\right) \times \\ & \times H\left(\frac{-\theta-\varphi}{2} - \frac{s}{4} - \frac{\gamma_\phi(s)}{2}\right) Q\left(\frac{\pi-\theta-\varphi}{2} - \frac{\gamma_\phi(s)}{2}\right) Q\left(\frac{\pi-\varphi}{2} - \frac{\gamma_\phi(s)}{2}\right) Q\left(-\frac{\pi}{4} - \frac{\gamma_\phi(s)}{2}\right), \end{aligned} \tag{5}$$

where $\gamma_\phi(s) = \phi - \alpha(s)$. We use this notation to emphasize that γ depends on both ϕ and s. Note that by going from Eq.(4) to Eq.(5) the gauge-fixing role – originally played by the plates implementing $V(\gamma)$ – turns to be shared by all the seven plates of the final array. The path followed by the polarization state subjected to U_{tot} can be represented on the Poincaré sphere by a circular arc, see Fig.(1). This arc is fixed by $\mathbf{n}(\theta, \varphi)$, by the initial polarization state, and by s. The latter fixes the angle by which the initial state is rotated. Once we have fixed $\mathbf{n}$ and the initial state, we record the geometric phase as a function of s. This is done by varying the registered intensity as a function of $\gamma_\phi(s)$, which plays a double role. First, it contains the phase-shift ϕ that is required to implement the polarimetric version of the Mach-Zehnder interferometer, as discussed above. Second, it contains the gauge-shift $\alpha(s)$ that is required to make the total phase coincide with the geometric phase. In order to extract this geometric phase, we project the state $U_n V(\gamma) |h\rangle$ onto the state $V(\gamma)|h\rangle = e^{-i\gamma/2}\left(|h\rangle - i e^{i\gamma}|v\rangle\right)/\sqrt{2}$. The recorded intensity is thus given by $I = \left|\langle h| V^\dagger(\gamma) U_n V(\gamma) |h\rangle\right|^2$. As we shall see, after having fixed θ, φ and s, we can let γ (viz. ϕ) vary so as to generate an intensity pattern $I(\phi)$, whose maxima and minima determine the value of the geometric phase at (s, θ, φ). This value can be compared with the theoretical one, which is given by $\Phi_g = \Phi_P - \Phi_{dyn}$, where

$$\Phi_P \;=\; \arg\langle\psi(0)|\psi(s)\rangle = \arg\langle h| U_n(s) |h\rangle = -\arctan\left[\sin\theta\cos\varphi\tan\left(\frac{s}{2}\right)\right], \tag{6}$$

$$\Phi_{dyn} \;=\; \Im\int_0^s \langle\psi(s)|\dot{\psi}(s)\rangle ds = \Im\int_0^s \langle h| U_n^\dagger(s)(-i\mathbf{n}\cdot\boldsymbol{\sigma}) U_n(s) |h\rangle\, ds = -\frac{s}{2}\langle h|\, \mathbf{n}\cdot\boldsymbol{\sigma}\, |h\rangle. \tag{7}$$

The theoretical expression for the geometric phase thus reads

$$\Phi_g^{th} = -\arctan\left[\sin\theta\cos\varphi\tan\left(\frac{s}{2}\right)\right] + \frac{s}{2}\sin\theta\cos\varphi. \tag{8}$$

On the other hand, a straightforward calculation of the intensity $I = \left|\langle h| V^\dagger\left(\phi - \alpha(s)\right) U_n(\theta, \varphi, s) V\left(\phi - \alpha(s)\right) |h\rangle\right|^2$ gives

$$I = \cos^2\left(\frac{s}{2}\right) + \sin^2\left(\frac{s}{2}\right)\left[\cos\theta\cos\left(\alpha(s) - \phi\right) + \sin\theta\sin\varphi\sin\left(\alpha(s) - \phi\right)\right]^2. \tag{9}$$

We have then,

$$I_{\min}(s) \;=\; \cos^2\left(\frac{s}{2}\right), \tag{10}$$

$$I_{\max}(s) \;=\; \cos^2\left(\frac{s}{2}\right) + \sin^2\left(\frac{s}{2}\right)\left[\cos^2\theta + \left(\sin\theta\sin\varphi\right)^2\right], \tag{11}$$

where we have used that the maximum of $f(\alpha) = a\cos\alpha + b\sin\alpha$ is given by $\sqrt{a^2+b^2}$. From the above equations we get

$$\frac{1-I_{\max}}{1-I_{\min}} = \sin^2\theta\cos^2\varphi, \tag{12}$$

$$\frac{1-I_{\max}}{I_{\min}} = \sin^2\theta\cos^2\varphi\tan^2\left(\frac{s}{2}\right). \tag{13}$$

We can thus express Φ_g^{th} in terms of the experimentally accessible quantities $I_{\min}$ and $I_{\max}$ as

$$\Phi_g(s) = \sqrt{\frac{1-I_{\max}(s)}{1-I_{\min}(s)}}\arccos\left[\sqrt{I_{\min}(s)}\right] - \arctan\left[\sqrt{\frac{1-I_{\max}(s)}{I_{\min}(s)}}\right], \quad \text{for } -\pi < s < \pi, \tag{14}$$

$$\Phi_g(s) = \sqrt{\frac{1-I_{\max}(s)}{1-I_{\min}(s)}}\arccos\left[-\sqrt{I_{\min}(s)}\right] + \arctan\left[\sqrt{\frac{1-I_{\max}(s)}{I_{\min}(s)}}\right] \pm \pi, \quad \text{for } \pi < s < 3\pi. \tag{15}$$

Note that Φ_g is undefined for $s = \pi$, cf. Eq.(8). The $\pm\pi$ that appears in $\Phi_g(s > \pi)$ comes from the Pancharatnam contribution, $\arg\langle h|\, U_n(s)\,|h\rangle$, that is contained in Φ_g^{th}. Indeed, $\langle h|\, U_n(s)\,|h\rangle = \cos(s/2)[1 - i\sin\theta\cos\varphi\tan(s/2)]$, so that $\arg\langle h|\, U_n(s)\,|h\rangle = \arg(\cos(s/2)) - \arctan[\sin\theta\cos\varphi\tan(s/2)]$. For $\pi < s < 3\pi$, we have that $\arg(\cos(s/2)) = \pm\pi$.

III. EXPERIMENTAL PROCEDURE AND ANALYSIS OF RESULTS

A sketch of our experimental arrangement is shown in Fig.(2). Its core is the array of seven plates that realize the transformation $U_{tot}(\theta, \varphi, \phi, s)$, as given in Eq.(5). Our single-photon source was a BBO crystal pumped by a cw diode laser (measured central wavelength: 400 nm, spectral line-width lies between 0.5 and 1 nm at operating temperatures; output power: 37.5 mW). Two photon beams were produced in the BBO crystal by type-I spontaneous parametric down-conversion, each beam having a wavelength of 800 nm. One beam, the idler or heralding one, was directed towards an avalanche photodetector. The other, signal beam, was directed towards the array of seven plates. Coincidence counts (I) of idler and signal beams made up our raw data, with coincidences being defined within a time-window of 10.42 ns. Our photon-counting module was a Perkin-Elmer SPCM-AQ4C, with a dark count-rate of 500 ± 10 cps. Photons were collected with the help of converging lenses that focused them into multimode fiber optic cables having fiber-coupling connectors at both ends. The recorded coincidences were obtained according to the following procedure. For given values of θ, φ and s, the seven plates were oriented as prescribed in Eq.(5), with $\gamma = \phi - s\sin\theta\cos\varphi/2$. The angle ϕ was varied from 0° to 360° in steps of 40°. Coincidence counts were recorded as a function of ϕ and then normalized to obtain the intensity $I(\phi)$. Theoretically, $I(\phi)$ is given by Eq.(9), with s, θ and φ being kept fixed. By repeated measurements we sampled 30 points for each value of ϕ. The parameter s took values s_i from 40° to 320° in steps of 40°. After averaging the recorded coincidence counts for each ϕ we obtained a series of points $I(\phi_i)$. A best fit $I(\phi)$ to these points was found, where $I(\phi)$ is a sinusoidal function whose parameters were fixed by the least squares method. Fig.(3) shows the so obtained curves for $\theta = \pi/2$, $\varphi = \pi/3$ and different values of s. From these curves we determined $I_{\max}$ and $I_{\min}$. Entering $I_{\max}$ and $I_{\min}$ in Eqs. (14) and (15), the experimental values of $\Phi_g(s, \theta, \varphi)$ can be obtained and compared with the ones predicted by Eq.(8). Fig.(4) shows our experimental results together with the corresponding theoretical predictions. As can be seen, two of the three cases seem to reflect a systematic departure of our experimental findings from the theoretical predictions. We will come back to this point below. As for the single-photon production, it was checked by the standard procedure [29, 30] of measuring the degree of second-order coherence, $g^{(2)}$, between the output fields of a beam-splitter, i.e., the reflected (R) and transmitted (T) beams. Detections at gates T and R were conditioned upon detection at a third gate G. In such a case, $g^{(2)} = P_{GTR}/(P_{GT}P_{GR})$, where the P_a denote probabilities for simultaneous detection at gates specified by label a. In terms of photocounts, N_a, the degree of coherence can be expressed as [31] $g^{(2)} = N_{GTR}N_G/(N_{GT}N_{GR})$. It has a value that is less than 1 for non-classical light. We obtained $g^{(2)} = 0.187 \pm 0.011$ in our experiments.

Several sources of experimental error could be identified. The main source of error came from the accuracy with which our plates could be oriented, i.e., $\pm 1°$ approximately. Another possible source of error came from our photons having a wavelength of 800 nm instead of the 808 nm that would be required for optimal performance of our wave plates. These are zero-order plates whose effective retardances at the produced wavelength made them slightly differ from being $\lambda/2$ and $\lambda/4$ plates. However, the corresponding departures (0.505λ instead of $\lambda/2$ and 0.253λ instead of $\lambda/4$) were small enough to be neglected as a sensible source of error. Accidental coincidence counts were also estimated to be too small (contribution to $g^{(2)}$ less than 0.19) for them to have a noticeable influence on the departures of our experimental findings from the theoretically predicted values when $s > \pi$ (see Fig.(4), middle and right panels). As

illustrated in Fig.(4), left panel, the agreement between theoretical predictions and measured values was very good. However, we also observed slight departures that occasionally increased. The dashed curves in Fig.(4), middle and right panels, correspond to the targeted geometric phase $\Phi_g(s,\theta,\varphi)$. Large departures seemed to reflect a drift of the measured values with respect to the assumed theoretical curve, rather than random fluctuations around this curve. In what follows, we substantiate our claim that the $\pm 1^\circ$ accuracy in the orientation of our plates does explain occasional, systematic departures of experimental measurements from theoretical predictions. Depending on the measured quantity, rotation errors of this magnitude can give rise to inaccuracies of various sorts, like those recently reported in [35]. It is important to identify error sources and their effects, specially when one's ultimate goal is to have a good understanding of how the geometric phase behaves in a noisy environment.

Let us denote by δ_i the departure of the i-th plate's orientation from its nominal value. For a quarter-wave plate we must then set $Q(x+\delta)$ instead of $Q(x)$ in Eq.(5). To first order in δ, we get $dQ(x) = Q(x+\delta) - Q(x) = \sqrt{2}i\delta R_x$, with

$$R_x = \begin{pmatrix} \sin(2x) & -\cos(2x) \\ -\cos(2x) & -\sin(2x) \end{pmatrix}. \tag{16}$$

Similarly, for a half-wave plate we obtain $dH(x) = H(x+\delta) - H(x) = 2i\delta R_x$. If we now replace the operators $Q(x)$ and $H(x)$ in Eq.(5) by $Q(x) + dQ(x)$ and $H(x) + dH(x)$, respectively, and then expand the result to first order in the δ_i, we obtain

$$U^\delta_{tot} = U_{tot} + \sum_{i=1}^{7} U^\delta_i, \tag{17}$$

where U^δ_i reads like U_{tot}, see Eq.(5), except that its i-th factor is replaced by $dH(x)$ when $i = 4$ and by $dQ(x)$ otherwise. U^δ_{tot} is then a function of all $\delta_{i=1,\ldots,7}$. From the amplitude $\langle h| U^\delta_{tot} |h\rangle$, we can calculate the total intensity $I_\delta = \left|\langle h| U^\delta_{tot} |h\rangle\right|^2$, once again to first order in the δ_i. With this expression, by choosing different values for the δ_i, we can study how much $I_\delta(\phi)$ differs from the $I(\phi)$ given in Eq.(9). We have found that the departures from I can be very sensitive to a change from, say, $\delta_i \approx +1^\circ$ to $\delta_i \approx -1^\circ$, keeping fixed all the other $\delta_{j\neq i}$. The values of $I_{\max}$ and $I_{\min}$ can be calculated using $I(\phi)$ and $I_\delta(\phi)$, in order to assess the sensitivity of the array to changes $\delta_i \approx \pm 1^\circ$ in the setting of the plates. The values of $I_{\max}$ and $I_{\min}$ that correspond to $I_\delta(\phi)$ show that inaccuracies $\delta_i \approx \pm 1^\circ$ can explain the observed differences between recorded phases and theoretically predicted ones, cf. Eqs. (14) and (15).

Last claim can be confirmed by the following, independent approach. Inaccuracies $\delta_i \approx \pm 1^\circ$ should translate into a departure of θ and φ from their nominal values. Let us then assume that our array does not realize the transformation $U_n(\theta,\varphi,s) = \exp\left[-is\mathbf{n}(\theta,\varphi)\cdot\boldsymbol{\sigma}/2\right]$, but instead $\exp\left[-is\mathbf{n}(\theta+\delta\theta,\varphi+\delta\varphi)\cdot\boldsymbol{\sigma}/2\right]$, with $\delta\theta \approx \pm 7^\circ \approx \delta\varphi$. The actual values of $\delta\theta$ and $\delta\varphi$ can be obtained by the following procedure. From Eq.(12) we see that $I_{\max}(s_i)$ and $I_{\min}(s_i)$ corresponding to targeted values θ and φ should satisfy

$$y(s_i) \equiv \frac{1 - I_{\max}(s_i)}{1 - I_{\min}(s_i)} = \sin^2\theta\cos^2\varphi \equiv f(\theta,\varphi). \tag{18}$$

The above equation can be used to determine the actual values of θ and φ, i.e., $\theta+\delta\theta$ and $\varphi+\delta\varphi$, by the least squares method. To this end, we evaluate the right-hand side of Eq.(18) in the sought-after values, expand it to first order, i.e., we set $f(\theta+\delta\theta,\varphi+\delta\varphi) = f(\theta,\varphi) + \left(\sin 2\theta\cos^2\varphi\right)\delta\theta - \left(\sin^2\theta\sin 2\varphi\right)\delta\varphi$, and then determine $\delta\theta$, $\delta\varphi$ as

$$\begin{pmatrix} \delta\theta \\ \delta\varphi \end{pmatrix} = \left(A^T W A\right)^{-1} A^T W b. \tag{19}$$

Here, $(\cdot)^{-1}$ means the Moore-Penrose pseudoinverse, b is the column vector $(y(s_i) - f(\theta,\varphi))^T$, with $i = 1,\ldots,n$ (n being the number of recorded points), A is the $n \times 2$ matrix whose rows are all equal to $(\sin 2\theta\cos^2\varphi, -\sin^2\theta\sin 2\varphi)$ and W is the inverse of the covariance matrix, i.e., $W = \mathrm{diag}(\sigma_1^{-2},\ldots,\sigma_n^{-2})$. The latter corresponds to statistically uncorrelated measurements having different variances σ_i at different values s_i. We have assessed these variances in two different ways. First, by fitting a Gaussian to the distributions of measured points, cf. Fig.(3), which gives us σ_i for each value $I(\phi_j)$ and hence for $I_{\min}$, $I_{\max}$, and Φ_g by error propagation. Second, from our raw data, which consists of 30 values for each ϕ_i – with s, θ, φ being kept fixed – we randomly chose 10 values for each ϕ_i and calculated Φ_g as we did when using the 30 values. By iterating this procedure several times (≈ 40), we got a series of values for each $\Phi_g(s,\theta,\varphi)$. From each series we obtained a mean value and its corresponding maximal and minimal departures. These departures constitute our error bars. Such an estimation is justified by the statistical independence of our measurements. Thus, randomly sampling 10 out of 30 measured values amounts to having recorded 10 values in each run of the experiment while repeating it several times (≈ 40). From the two methods we observe that our measured

values σ_i span a range that goes from a minimum of 1.3×10^{-4} to a maximum of 0.12. The plotted error bars, cf. Fig(4), are mostly smaller than the symbols and can be barely seen only in cases for which $\sigma_i \approx 0.1$. Now, the above mentioned application of the least squares method holds whenever inaccuracies δs_i of the s_i can be neglected. In our case, the nominal value of s enters in the orientations of our wave plates, and the inaccuracies of these orientations are precisely the assumed main source of errors. Nevertheless, the above application of the least squares method is justified. Indeed, we can assess the values of the δs_i by using Eq.(10). That is, we set $\delta s_i \approx \left| s_i - 2 \arccos\left(\sqrt{I_{\min}(s_i)}\right)\right|$ as an estimator of the inaccuracies of the s_i. These inaccuracies turn out to be negligible in comparison to our σ_i – besides, if they were not, they would modify the above results only to higher order than the first in $(\delta\theta, \delta\varphi)$, because our $y(s_i)$ do not depend on s, as Eq.(18) shows. The least squares method can thus be iteratively applied to find successive values of $\delta\theta$ and $\delta\varphi$, until $\Phi_g^{th}(s, \theta + \delta\theta, \varphi + \delta\varphi)$ of Eq.(8) eventually matches experimental results. In the present case, however, it proved more practical to seek the right choice of θ and φ by hand, i.e., by trial and error when plotting $\Phi_g^{th}(s, \theta + \delta\theta, \varphi + \delta\varphi)$ together with its measured values. Indeed, by so doing in the cases of Fig.(4), middle and right panels, we quickly found values $\delta\theta \approx \pm 7^\circ \approx \delta\varphi$ for which the theoretical curves approximate very closely our experimental results. Fig.(4) shows the curves obtained with $\delta\theta = 3^\circ$, $\delta\varphi = -7^\circ$ (middle panel) and $\delta\theta = 5^\circ$, $\delta\varphi = -4^\circ$ (right panel). Such a result is consistent with the assumed errors $\delta_i \approx \pm 1^\circ$, which may accumulate so as to produce inaccuracies $\delta\theta \approx \pm 7^\circ \approx \delta\varphi$. Thus, departures of θ and φ from their targeted values do explain our experimental findings. We have thereby assessed the amount by which the theoretically predicted value $\Phi_g^{th}(s, \theta, \varphi)$ might differ from the experimentally realized one. Such a difference should be taken into account when assessing with the help of a polarimetric array the robustness of Φ_g against decohering mechanisms.

Finally, let us point out the following feature of our array. As can be seen from Eqs.(14) and (15), the geometric phase we produce depends on θ and φ only through $|\sin\theta\cos\varphi|$. This means that we can fix the actually realized values of θ and φ only up to changes $(\theta, \varphi) \to (\theta', \varphi')$ that leave $|\sin\theta\cos\varphi|$ invariant. Instead of seing this as a weakness of our approach, such a feature can be helpful when seeking to exploit the robustness of Φ_g against decoherence. Indeed, if one is able to confine decohering effects to those regions in the plane (θ, φ) for which the variations in $|\sin\theta\cos\varphi|$ are sufficiently small, then Φ_g will vary also within acceptable limits. Of course, these limits will depend on the application one has in mind and on the decohering mechanisms, which should be studied in detail. Such an endeavor goes beyond the scope of the present paper and is deferred to future work.

IV. CONCLUSIONS

Our polarimetric setup proved to be a versatile tool for testing geometric phases. The main part of it, an array made of one $\lambda/2$ and six $\lambda/4$ plates, allows us to realize geometric phases that are associated to non-geodesic paths on the Poincaré sphere. Although we have limited ourselves to study circular trajectories, our approach can be extended to deal with arbitrary paths. Our experimental results fit very closely theoretical predictions, once we have accurately identified the trajectory on the Poincaré sphere that has been actually realized by our setting. The end product of such a setting is a geometric phase Φ_g that is non-trivially related to various parameters entering our setup. Indeed, coincidence counts must be optimized by adjusting the laser polarization, the acquisition window for photon counts must also be properly fixed, and the wave plates must be repeatedly set to their nominal orientations when recording the data from which Φ_g can be extracted. Not only because of the photon counting statistics, but mainly because of our $\pm 1^\circ$ accuracy in the setting of the plates, one could expect experimental results falling within some region around the theoretical curves, as reported, e.g., in [35]. If that would have been the case, our polarimetric array would have proved inappropriate for studying robustness of geometric phases against noise. However, our array does produce geometric phases that are in accordance with theoretical expressions. Occasionally, these expressions must be evaluated *a posteriori*, thereby identifying the actually realized values of the parameters fixing Φ_g. Once the value of Φ_g has been fixed, our array could be used for assessing the robustness of this Φ_g against noise. To this end, the array must be complemented so as to simulate different kinds of noise. For instance, one can replace the single-crystal photon's source and use instead polarization-entangled photons produced by parametric down-conversion in a two-crystal geometry [32, 33]. This produces variable entangled polarization states. After tracing over the polarization of one of these photons, its twin photon is brought into a mixed polarization state $\rho = (\mathbb{1} + r\mathbf{n}\cdot\boldsymbol{\sigma})/2$, with $r \in [0, 1]$ being the degree of polarization. Such a state can be submitted to a polarimetric array similar to the one discussed in this paper. Now, ρ can be written in the form $\rho = \lambda_+ |\mathbf{n}_+\rangle\langle\mathbf{n}_+| + \lambda_- |\mathbf{n}_-\rangle\langle\mathbf{n}_-|$, with $\lambda_\pm = (1 \pm r)/2$ and $\mathbf{n}\cdot\boldsymbol{\sigma}\,|\mathbf{n}_\pm\rangle = \pm\,|\mathbf{n}_\pm\rangle$. Applying to $|\mathbf{n}_\pm\rangle$ the techniques of the present work one can get the corresponding (pure-state) geometric phases $\pm\Phi_g$. This is all one needs [34] to obtain the geometric phase of the mixed-state ρ, thereby assessing the effect of noise. Experiments along these lines have been already performed in neutron polarimetry [17, 18]. The kind of noise studied in [17] translated into a Stokes vector $\mathbf{r} = r\mathbf{n}$ of the restricted form $\mathbf{r} = (0, -r, 0)$, and the explored paths on the Bloch sphere originated from unitary transformations that depended on two of the three Euler angles [17]. By appropriate choice of these two angles one can generate purely geometric, purely dynamical,

or combinations of both phases. However, once this choice is made, one cannot freely address different paths on the Bloch sphere. Nevertheless, these results represented a considerable extension of previous ones [15], which dealt with Pancharatnam's phase only. Further progress in assessing the robustness of geometric phases was achieved by addressing adiabatic evolutions [18]. Here, the dynamical contribution to the total phase was eliminated by spin-echo techniques, which impose some restrictions on the class of paths being explored. Our all-optical setting offers some advantages as compared to neutron polarimetry. It allows choosing arbitrary paths on the Poincaré sphere, as well as different kinds of noise to be explored in conjunction with the chosen path. The aforementioned remote state preparation of mixed states is not the only choice. One can also employ interferometric techniques to produce an enlarged family of mixed states [35, 36]. By applying interferometry for input-state preparation and polarimetry for state manipulation, one has the possibility of studying the resilience of purely geometric phases to various types of noise.

V. ACKNOWLEDGEMENTS

This work was partially financed by DGI-PUCP (Grant No. 2013-0130). J. C. S. thanks E. J. Galvez for support and advice during his stay at Colgate University.

[1] M. V. Berry, Proc. R. Soc. London Ser. A **392**, 45 (1984).
[2] J. H. Hannay, J. Phys. A **18**, 221 (1985).
[3] D. M. Tong, E. Sjöqvist, L. C. Kwek, and C. H. Oh, Phys. Rev. Lett. **93**, 080405 (2004).
[4] J. G. Peixoto de Faria, A. F. R. de Toledo Piza, and M. C. Neves, Europhys. Lett. **62**, 782 (2002).
[5] F. M. Cucchietti, J.-F. Zhang, F. C. Lombardo, P. I. Villar, and R. Laflamme, Phys. Rev. Lett. **105**, 240406 (2010).
[6] A. Uhlmann, Rep. Math. Phys. **24**, 229 (1986).
[7] E. Sjöqvist, A. K. Pati, A Ekert, J. S. Anandan, M. Ericsson, D. K. L. Oi, and V. Vedral, Phys. Rev. Lett. **85**, 2845 (2000).
[8] K.-P. Marzlin, S. Ghose, and B. C. Sanders, Phys. Rev. Lett. **93**, 260402 (2004).
[9] A. Bassi and E. Ippoliti, Phys. Rev. A **73**, 062104 (2006).
[10] A. T. Rezakhani and P. Zanardi, Phys. Rev. A **73**, 052117 (2006).
[11] S. Yin and D. M. Tong, Phys. Rev. A **79**, 044303 (2009).
[12] N. Burić and M. Radonjić, Phys. Rev. A **80**, 014101 (2009).
[13] F. Lombardo and P. I. Villar, Phys. Rev. A **81**, 022115 (2010).
[14] E. Sjöqvist, Physics **1**, 35 (2008).
[15] J. Klepp, S. Sponar, Y. Hasegawa, E. Jericha, G. Badurek, Phys. Lett. A **342**, 48 (2005).
[16] R. Bertlmann, K. Durstberger, Y. Hasegawa, and B. C. Hiesmayr, Phys. Rev. A **69**, 032112 (2004).
[17] J. Klepp, S. Sponar, S. Filipp, M. Lettner, G. Badurek, and Y. Hasegawa, Phys. Rev. Lett. **101**, 150404 (2008).
[18] S. Filipp, J. Klepp, Y. Hasegawa, C. Plonka-Spehr, U. Schmidt, P. Geltenbort, and H. Rauch, Phys. Rev. Lett. **102**, 030404 (2009).
[19] S. Werner, Found. Phys. **42**, 122 (2012).
[20] A. G. Wagh and V. C. Rakhecha, Phys. Lett. A **197**, 112 (1995).
[21] S. Sponar *et al.*, New J. Phys. **14**, 053032 (2012).
[22] N. Mukunda and R. Simon, Ann. Phys. (N. Y.) **228**, 205 (1993).
[23] S. Pancharatnam, Proceedings of the Indian Academy of Science A **44**, 247 (1956).
[24] J. Audretsch, *Entangled systems: new directions in quantum physics* , Wiley-VCH, Chichester (2007).
[25] J. C. Loredo, O. Ortíz, R. Weingärtner, and F. De Zela, Phys. Rev. A **80**, 012113 (2009).
[26] J. C. Loredo, O. Ortíz, A. Ballón, and F. De Zela, J. of Phys.: Conf. Ser. **274**, 012140 (2011).
[27] J. C. Loredo, Master Thesis, Physics Section, Pontificia Universidad Católica del Perú, Lima-Peru (2011).
[28] R. Simon and N. Mukunda, Phys. Lett. A **138**, 474 (1989).
[29] P. G. Kwiat and R. Y. Chiao Phys. Rev. Lett. **66**, 588 (1991).
[30] J. J. Thorn, M. S. Neel, V. W. Donato, G. S. Bergreen, R. E. Davies, and M. Beck, Am. J. Phys. **72**, 1210 (2004).
[31] P. Grangier, G. Roger, and A. Aspect, Europhys. Lett. **1**, 173 (1986).
[32] P. Kwiat, E. Waks, A. G. White, I. Appelbaum, and P. H. Eberhard, Phys. Rev. A **60**, R773 (1999).
[33] S. P. Walborn, C. H. Monken, S. Pádua, and P. H. Souto Ribeiro, Phys. Rep. **495**, 87 (2010).
[34] P. Larsson and E. Sjöqvist, Phys. Lett. A **315**, 12 (2003).
[35] K. A. G. Fisher, R. Prevedel, R. Kaltenbaek, and K. J. Resch, New J. Phys. **14**, 033016 (2012).
[36] F. De Zela, J. Opt. Soc. Am. A **30** 1544 (2013).

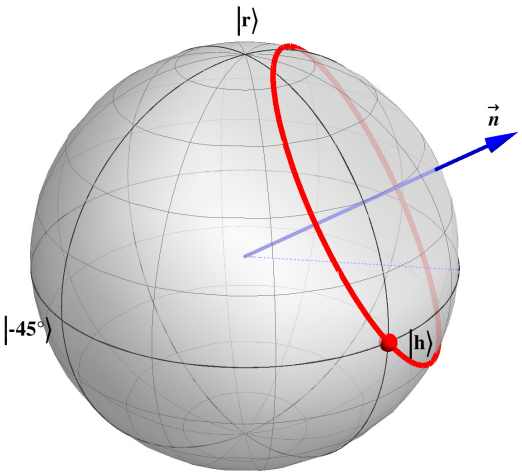


Figure 1: (Color online) Path followed on the Poincaré sphere by the Stokes vector that corresponds to an initial state $|h\rangle$ being submitted to a transformation $\exp(-is\mathbf{n}\cdot\boldsymbol{\sigma}/2)$. The rotation axis $\mathbf{n}$ has polar angles $\theta = \pi/3, \varphi = \pi/4$. The dynamical contribution to the total phase Φ_P is gauged-away all along the curve, so that $\Phi_P = \Phi_g$ holds at each value of s.

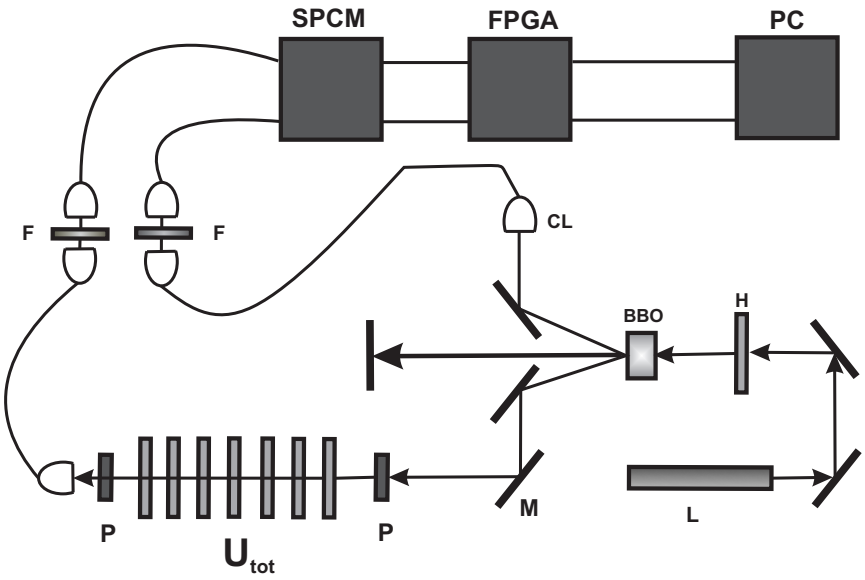


Figure 2: Polarimetric array. The set of seven wave plates shown at the bottom can be oriented so as to realize the desired $SU(2)$ transformation (U_{tot}) in polarization space. Polarized photons enter this array after having been produced in a non-linear, beta-barium borate crystal (BBO) that is fed by a diode laser (L) that emits 400 nm light whose polarization is fine-tuned with a $\lambda/2$ plate (H) placed before the crystal. Polarizers (P) set before and after the retarders project the photon's polarization as required (see text). Signal photons are recorded in coincidence with their heralding twins in a single-photon counting module ($SPCM$). Other components are M: mirrors, CL: converging lenses, F: filters, $FPGA$: field programmable gate array, PC: personal computer.

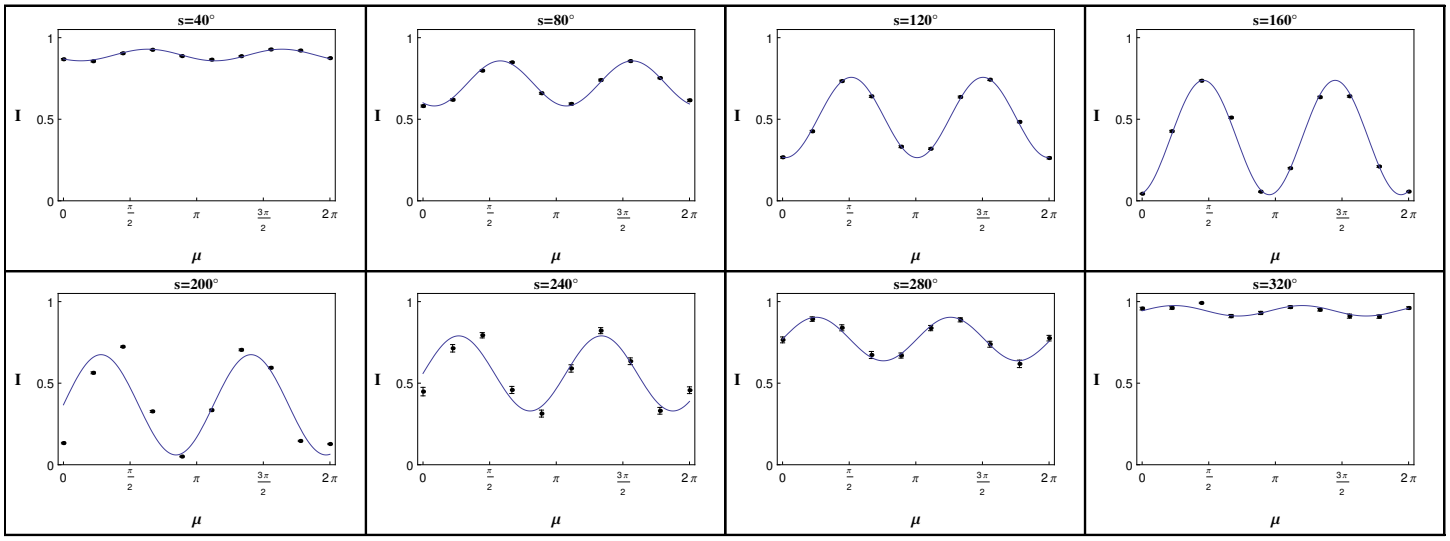


Figure 3: (Color online) The geometric phase is experimentally fixed by the maxima and minima of the measured curves $I_{exp}(\phi)$. The plotted curves correspond to $\theta = \pi/3$, $\varphi = \pi/3$.

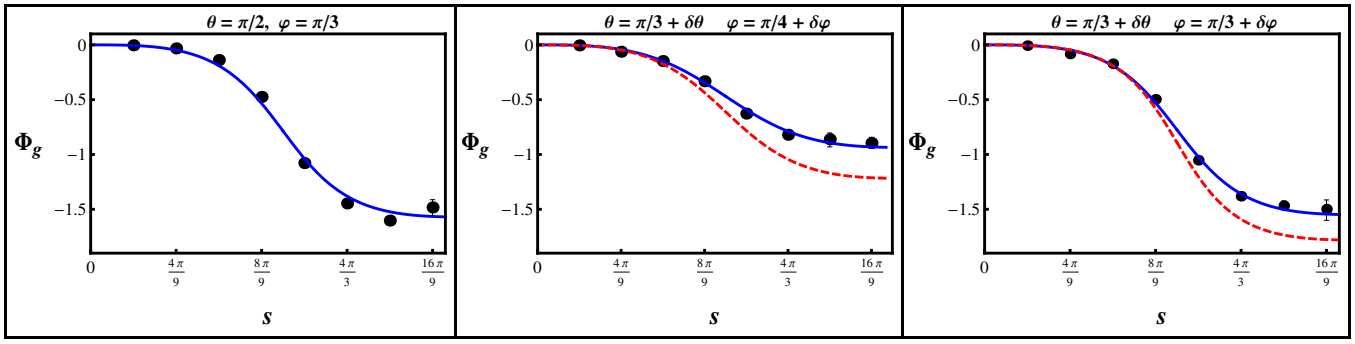


Figure 4: (Color online) Geometric phase $\Phi_g(s, \theta, \varphi)$ as a function of parameter s for three choices of (θ, φ). Curve $\Phi_g(s, \pi/2, \pi/3)$ closely matches experimental results. However, $\Phi_g(s, \pi/3, \pi/4)$ and $\Phi_g(s, \pi/3, \pi/3)$ seem to systematically deviate from the measured values. By properly identifying the actual values of (θ, φ), the theoretical curves do match experimental results. Dashed curves correspond to $\Phi_g(s, \pi/3, \pi/4)$ (middle panel) and to $\Phi_g(s, \pi/3, \pi/3)$ (right panel). Full curves correspond to $\Phi_g(s, \pi/3 + \delta\theta, \pi/4 + \delta\varphi)$ with $\delta\theta = 3^\circ\pi/180^\circ$, $\delta\varphi = -7^\circ\pi/180^\circ$ (middle panel) and to $\Phi_g(s, \pi/3 + \delta\theta, \pi/3 + \delta\varphi)$ with $\delta\theta = 5^\circ\pi/180^\circ$, $\delta\varphi = -4^\circ\pi/180^\circ$ (right panel). Most error bars are smaller than symbols.